Research Article Vol. 32, No. 4 / 12 Feb 2024 / Optics Express 5898
Optics EXPRESS

Quantum ghost imaging of a vector field

ZHI-XIANG LI,[1] DONG ZHU,[1] JIANG-SHAN TANG,[1] MING-YUAN CHEN,[1] YA-PING RUAN,[1] JIAN-JI LIU,[2] HAN ZHANG,[3] PENG CHEN,[1] KE-YU XIA,[1,4] LI-JIAN ZHANG,[1,5] AND YAN-QING LU[1,6]

[1]*National Laboratory of Solid State Microstructures, College of Engineering and Applied Sciences, and Collaborative Innovation Center of Advanced Microstructures, Nanjing University, Nanjing 210093, China*
[2]*State Key Laboratory of Precision Spectroscopy, East China Normal University, Shanghai 200062, China*
[3]*School of Physics, Nanjing University, Nanjing 210023, China*
[4]*keyu.xia@nju.edu.cn*
[5]*lijian.zhang@nju.edu.cn*
[6]*yqlu@nju.edu.cn*

Abstract: Quantum ghost image technique utilizing position or momentum correlations between entangled photons can realize nonlocal reconstruction of the image of an object. In this work, based on polarization entanglement, we experimentally demonstrate quantum ghost imaging of vector images by using a geometric phase object. We also provide a corresponding theoretical analysis. Additionally, we offer a geometrical optics path explanation of ghost imaging for vector fields. The proposed strategy offers new insights into the fundamental development of ghost imaging and also holds great promise for developing complex structured ghost imaging techniques. Our work expanding the principle of ghost imaging to spatially varying vector beams will lead to interesting developments of this field.

1. Introduction

Ghost imaging is a fascinating technique that allows the reconstruction of images without direct interaction with the object. Ghost imaging has seen significant growth in the past years [1,2]. It has found applications ranging from microscopy [3], three-dimensional ghost imaging [4,5], naked-eye ghost imaging [6] to cryptography [7], etc. Ghost imaging demonstrated with X-rays [8,9], atoms [10] and even electrons [11] extend this technique to broader research areas.

Quantum ghost imaging uses quantum entangled light sources to image objects. Its history dates back to the early 90s of the 20th centuries, when Shih and co-workers first demonstrated the ghost imaging of amplitude objects [12,13], following the theoretical work by Klyshko [14]. Advantageously, the use of quantum light allows for imaging at low light levels, demonstrating a higher signal-to-noise ratio. Particularly, it is useful for biological imaging applications as it reduces the risk of photodamage to light-sensitive matter. In early quantum ghost imaging experiments, researchers used two-photon entangled light sources. This light source produced a pair of highly correlated photons, one of which was sent to the object, scattered and received by the detector, and the other photon was sent to the scanning imaging detector [15]. By measuring and analyzing a large number of photon pairs, the researchers were able to restore images of objects. Nowadays, the time-gated camera provides a direct way to observe the two-dimensional distribution of ghost imaging. Additionally, it increases the detection efficiency of a ghost imaging system [16,17]. In recent years, by exploiting hyperentanglement, multichannel parallel ghost imaging has been realized [18]. Chen et.al implemented quantum-correlation-based human face recognition [19]. A super-resolved imaging approach based on neural networks was also been studied [20]. These studies have laid the foundation for the development and application of quantum ghost imaging technology, and have important significance in the field of quantum imaging.

#508060 https://doi.org/10.1364/OE.508060
Journal © 2024 Received 25 Oct 2023; revised 21 Dec 2023; accepted 19 Jan 2024; published 5 Feb 2024

Optics EXPRESS

Despite the progress in ghost imaging of amplitude objects, imaging of optical phase information has progressed slowly. Phase objects in optics usually refer to objects where the phase information of light waves changes. For a pure phase object, the ghost diffraction pattern of the phase object has been used to detect the phase spatial distribution, using quantum entanglement [4] or pseudothermal light [21]. In 2016, the position and orbital angular momentum (OAM) correlations between the entangled photons were used to obtain ghost images of a phase object [22]. In 2019, based on an interferometric approach, in an interaction-free ghost-imaging scheme, imaging of structured objects and simple phase objects was demonstrated [23]. Moreover, quantum ghost imaging of a transparent polarisation sensitive phase pattern was realized [24]. Recently, Sephton et.al proposed a novel method to obtain the full phase and amplitude information of complex objects through single-pixel quantum ghost imaging [25]. In their work, two image reconstructions (cosine and sine) are required to fully reconstruct a phase object.

Ghost imaging of polarization information has also attracted increasing attention in the past several years. Kellock et.al proposed polarimetry by classical ghost diffraction [26] to retrieve the Jones matrix of the polarization object. Polarization ghost imaging using classical light was proposed [27–29], and it is usually used to retrieve the image when the object is buried in the background of different polarization properties. This is useful in discriminating the object from the different material background. Later, a ghost polarization communication scheme between two parties was developed [30]. Vega et.al presented the quantum ghost discrimination of three different simple polarization objects [31]. Quantum ghost polarimetry with entangled photons was verified lately [32].

Vector beams, where the light polarization in the transverse plane is space-variant, have various applications from microscopy and imaging, to quantum cryptography and computing [33–35]. To date, to the best of our knowledge, there is no investigation about quantum imaging of vector beams. Investigating the quantum ghost imaging of vector filed could enable the ghost imaging of complex structured field. Moreover, it may have application in imaging universal motion vectors in the natural world.

In this work, we demonstrate ghost imaging of vector vortex distribution by using polarization entanglement. Generally, the ghost imaging does work is solely a result of the correlation between the transverse spatial position or momentum correlation of the signal and idler photons. Our results show that polarization entanglement plays a key role in the ghost imaging of vector beams. Quantum ghost imaging of vector beams adds an extra dimension to ghost imaging, which could further be used to increase the amount of information that can be captured and transmitted.

2. Experiments

We use a geometric phase object with spatially varying optical axes orientation - a liquid crystal q-plate - as the object. Q-plate is a birefringent wave plate with an inhomogeneous distribution of the local optical axis in the transverse plane and the pattern of the optical axis distribution is defined by a topological charge "q", which can be an integer or half-integer. When a circularly polarized light beam passes through a q-plate, $2q\hbar$ amount of OAM is transferred into the beam, with the sign determined by the input polarization helicity [36,37]. For circularly polarized photons, the q-plate performs the transformation $|R, 0\rangle \rightarrow |L,\ -2q\rangle$ and $|L, 0\rangle \rightarrow |R,\ 2q\rangle$. Here we denote polarization and OAM information of photons as $|p, m\rangle$. In our experiment, we use a q-plate with $q = 0.5$. We define the operator of the q-plate as $\hat{Q}$. For horizontally polarized $|H\rangle = \frac{1}{\sqrt{2}}(|L\rangle + |R\rangle)$ state and vertically polarized $|V\rangle = \frac{-i}{\sqrt{2}}(|L\rangle - |R\rangle)$ state,

$$\hat{Q}|H,\ 0\rangle \rightarrow \frac{1}{\sqrt{2}}(|R,\ 1\rangle + |L,\ -1\rangle), \tag{1}$$

$$\hat{Q}|V,\ 0\rangle \rightarrow \frac{-i}{\sqrt{2}}(|R,\ 1\rangle - |L,\ -1\rangle). \tag{2}$$

Optics EXPRESS

Equation (1) and (2) represent radically polarized and azimuthally polarized vector vortex state, respectively.

In our experiment, polarization-entangled photons are generated via the spontaneous parametric down-conversion process based on a PPKTP Sagnac interferometer scheme [38,39]. First, we place an electron-multiplying CCD (EMCCD) in the object arm to observe the photon distribution after the direct interaction with q-plate. The experimental setup is given in Fig. 1(a). The photons from the entanglement source consist both H and V polarizations. If we select a linearly polarized component H with polarizer P1, after interaction with the q-plate, we get a vector vortex beam as predicted by Eq. (1). By rotating another polarizer P2 placed after the q-plate, we can see the corresponding distribution of the vector beam, as shown in Fig. 1(b). When the image is recorded using a single polarizer P1 or P2, it results in a donut shape. The results are shown in Fig. 1(c) and (d).

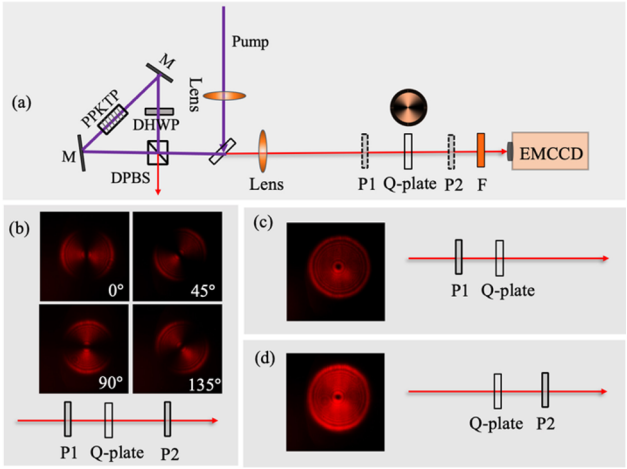

Fig. 1. The directly measured photon distributions in the object arm by an EMCCD. (a) The experimental setup. (b) Photon distribution images with two polarizers, one polarizer placed before the q-plate and the other after the q-plate. The second polarizer P2 is rotated (0°, 45°, 90°, 135°). (c) Photon distribution with only one polarizer, placed before the q-plate. (d) Photon distribution with only one polarizer, placed after the q-plate.

Next, we investigate the ghost imaging of the spatially varying distribution of vector vortex. We illustrate the scheme in Fig. 2. We prepared the photon pairs in the state of $\psi_P = \frac{1}{\sqrt{2}}(|H\rangle|H\rangle - |V\rangle|V\rangle)$ [39]. The coincidence count rate is measured to be 8 kHz. The photon pairs are split and propagate through the object and imaging arms. We also measured the second-order correlation function $g^2(\tau)$ of our quantum system. $g^2(\tau)$ describes the time dependent second-order coherence of the entangled photons. The result is given in Fig. 4, one can see that the $g^2(0)$ is approaching zero. $g^2(0)$ is interpreted as the probability of detection of two photons in the signal arm at the same time when the object photon is detected. Thus, each time a photon is detected, at the exact time, there is only one photon in the image arm, which proves that we used indeed correlated photons. The experimental method can be found in Ref. [40]. Both the q-plate and a gated intensified CCD (ICCD) are placed at the Fourier plane of the output plane of the PPKTP crystal. The photons that pass through the object are then collected by a fiber port coupler into a single-mode fiber. The optical fiber connects a single-photon counting module (SPCM). The detections of the photons in the object arm by the SPCM are used to trigger ICCD for the acquisition of ghost images. The photon counts registered in the object arm by the SPCM give no spatial information about the phase object. The photons in the imaging arm

Optics EXPRESS

collected by the ICCD, which have never interacted with the object, form the ghost image of the distribution of signal photons at the output plane of the object, i.e., right after the interaction of the q-plate.

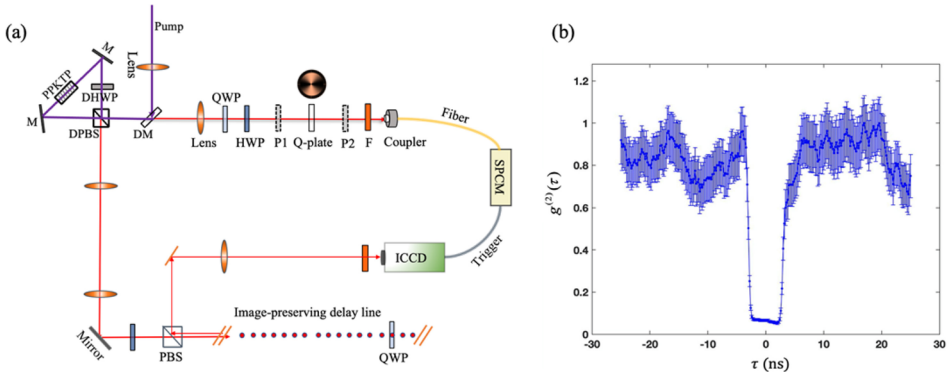

Fig. 2. (a) Experimental setup of ghost imaging. The image-preserved delay line consists of 12 lenses with a focal length of $f = 500$ mm and 14 mirrors in a double-pass configuration. QWP: Quarter-wave plate; HWP: half-wave plate; P: polarizer; F: filter. (b) The measured second-order coherence function $g^2(\tau)$ with 5 ns coincidence window. The experimental setup to measure $g^2(\tau)$ can be found in Ref. [40].

To compensate for the delay of the triggering mechanism of ICCD and the length of optical fiber we build an image-preserved delay line of 25 meters. The optical delay line is set in a double-pass configuration. This delay line contains twelve lenses with 500 mm focal length; the overall transmission efficiency of the optical path is about 30%. The ICCD is set at fast external mode with an optical gate width of 5 ns. The triggering mechanism of the ICCD leads to a 70 ns delay, while the overall optical length of the image-preserving delay line is 25 m, an additional optical delay of the ICCD is adjusted to ensure the of the synchroneity of entangled photons. We acquired the triggered ghost images based on an accumulation of 600 images with each exposure time being 1s. For our quantum ghost imaging scheme, the noise level is suppressed because the ICCD camera is triggered only when a photon is detected in the object arm within a very small gate width.

To obtain the spatially varying vector distribution in the imaging arm, the polarization information must be considered during the ghost imaging process. First, consider the scenario of selecting linearly polarized photons in the object arm right before the q-plate. We put a polarizer P1 before the q-plate to allow H-polarized light to pass. Photons in the imaging arm collapse into H-polarized photons. The ghost image collected by the ICCD is given in Fig. 3(a). Figure 3(b) is the simplified experimental scheme of the polarization elements in both arms.

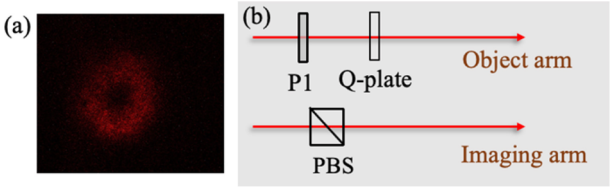

Fig. 3. The observed ghost images with a polarizer placed before q-plate in the object arm. (a) Ghost image distribution with no polarizer placed before ICCD, with $m = 1$. (b) The corresponding experimental scheme of polarization elements.

Optics EXPRESS

For a pump beam with zero angular momentum, the emitted entangled spatial state can be represented by the superposition of different OAMs [41]:

$$\psi_s = c_{0,0}|0\rangle_1|0\rangle_2 + c_{1,-1}|1\rangle_1|-1\rangle_2 + c_{-1,1}|-1\rangle_1|1\rangle_2 + c_{2,-2}|2\rangle_1|-2\rangle_2 + c_{-2,2}|-2\rangle_1|2\rangle_2 + \ldots. \quad (3)$$

Here the numbers in the brackets represent the indices m of the OAM modes, $c_{\mathrm{i,j}}$ denote the corresponding probability amplitude for measuring $|i\rangle|j\rangle$. As the photons in the object arm are collected by single-mode fibers, for our experiments with $q = 0.5$, only OAM modes with topological charge of $m = 1$ and $m = -1$ will contribute to the final outcome. The entanglement of polarization and spatial OAM mode can be written as

$$\psi_0 = \tfrac{1}{\sqrt{2}}\left(|H\rangle_1|H\rangle_2 - |V\rangle_1|V\rangle_2\right) \otimes \psi_s = \tfrac{1}{\sqrt{2}}\left(c_{1,-1}|H,1\rangle_1|H,-1\rangle_2 + c_{-1,1}|H,-1\rangle_1|H,1\rangle_2\right) - \tfrac{1}{\sqrt{2}}\left(\left(c_{1,-1}|V,1\rangle_1|V,-1\rangle_2 + c_{-1,1}|V,-1\rangle_1|V,1\rangle_2\right)\right. . \quad (4)$$

After the interaction with polarizer P1, the photons in the object arm are projected into H polarization state. The biphoton state becomes

$$\psi_{\mathrm{P1}} = \frac{1}{\sqrt{2}}(c_{1,-1}|H,1\rangle_1|H,-1\rangle_2 + c_{-1,1}|H,-1\rangle_1|H,1\rangle_2). \quad (5)$$

The action of q-plate on H linearly polarized states with arbitrary OAM m can be written as

$$\hat{Q}|H,\ m\rangle \rightarrow \frac{1}{\sqrt{2}}(|R,\ m+1\rangle + |L,\ m-1\rangle). \quad (6)$$

Thus, after the q-plate, the state becomes

$$\psi_{\mathrm{QP1}} = \hat{Q}\,\psi_{\mathrm{P1}} = \frac{1}{\sqrt{2}}c_{1,-1}(|L,0\rangle_1 + |R,2\rangle_1)|H,-1\rangle_2 + \frac{1}{\sqrt{2}}c_{-1,1}(|L,-2\rangle_1 + |R,0\rangle_1)|H,+1\rangle_2. \quad (7)$$

The final state after interaction with the q-plate and the single mode fiber $|0\rangle\langle 0|$ becomes

$$\psi_{\mathrm{f1}} = \frac{1}{\sqrt{2}}c_{1,-1}|L,0\rangle_1|H,-1\rangle_2 + \frac{1}{\sqrt{2}}c_{-1,1}|R,0\rangle_1|H,+1\rangle_2. \quad (8)$$

The OAM of the photons in the imaging arm are in a mixture state of $|-1\rangle$ and $|1\rangle$. This corresponds to a donut distribution. The experimental result in Fig. 3(a) is consistent with the theoretical analysis.

Then, we consider a different setting of the polarizer. We put a polarizer P2 after the q-plate in the object arm, and P1 is removed. This time, the polarization entanglement is well preserved when the photons reach at the q-plate. After the q-plate, the state become

$$\psi_{\mathrm{QP2}} = \hat{Q}\psi_0 = \hat{Q}\left(\frac{1}{\sqrt{2}}(|H\rangle_1|H\rangle_2 - |V\rangle_1|V\rangle_2) \otimes \psi_s\right) = \hat{Q}\left(\frac{1}{\sqrt{2}}(|R\rangle_1|R\rangle_2 + |L\rangle_1|L\rangle_2) \otimes \psi_s\right). \quad (9)$$

Simplifying the formula, we get

$$\psi_{\mathrm{QP2}} = \frac{1}{\sqrt{2}}\left(c_{1,-1}|L,0\rangle_1|R,-1\rangle_2 + c_{-1,1}|L,-2\rangle_1|R,1\rangle_2 + c_{1,-1}|R,2\rangle_1|L,-1\rangle_2 + c_{-1,1}|R,0\rangle_1|L,1\rangle_2\right). \quad (10)$$

We define the projection operator of the polarizer with an angle α as

$$P_\alpha = |\alpha\rangle\langle\alpha|, \quad (11)$$

Optics EXPRESS

with $|\alpha\rangle = \cos\alpha|H\rangle + \sin\alpha|V\rangle$. After the interaction with polarizer P2 and the single-mode fiber, the final state becomes

$$\psi_{f2} = \frac{c}{\sqrt{2}}(e^{i\alpha}|\alpha,0\rangle_1|R,-1\rangle_2 + e^{-i\alpha}|\alpha,0\rangle_1|L,1\rangle_2), \tag{12}$$

where we assume $c_{1,-1} = c_{-1,1} = c$. If P2 is set at an arbitrary polarization angle $|\alpha\rangle|0\rangle$, the photon state in the imaging arm can be written as $e^{i\alpha}|R\rangle|-1\rangle + e^{-i\alpha}|L\rangle|1\rangle$, which corresponds to a vector vortex beam [42,43]. The PBS in the imaging arm allows H polarized state to pass, therefore one can obtain a two-petal distribution as shown in Fig. 4(a). As the polarization angle α of P2 changes, we observed the corresponding rotation of the image. The results are given in Fig. 4(b)-(d). Our experimental results verified the vector nature of the ghost imaging. Compare Fig. 1(d) with Fig. 4, we can see that the ghost imaging of the vector beam is not just a result of the position correlation, the polarization correlation plays a key role here.

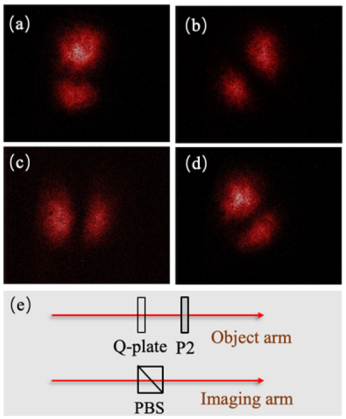

Fig. 4. The observed ghost images of $m = 1$ with a polarizer placed after the q-plate. (a)–(d) The observed photon distributions of the ghost vector-vortex beam as the polarization angle of P2 is 0°, 45°, 90° and 135°, separately. (e) Experimental setting of polarizers.

The directly measured photon distributions of the object shown in Fig. 1(b) and the ghost images in Fig. 4 are slightly different, and this is mainly due to the different resolution limit of the two systems. The photons in the object arm generated from spontaneous parametric down-conversion process interact directly with the q-plate. The resolution of the directly recorded images is solely affected by effective aperture of the optical elements in the optical path. While for the ghost images, the resolution of the ghost images depends on the strength of the correlation between the photons and the resolution of the whole quantum system. Compared with the direct imaging, the effective aperture of the system and the entanglement correlation causes a degradation of resolution. Despite the differences caused by the system resolution, both the ghost images and the directly obtained images show the vector properties of the vector field. Hence the results verify the successful generation of vector ghost field.

To show the feasibility of the scheme, we further investigate another vector mode with the topological value $m = 2$. The results are given in Fig. 5. Figure 5(a) is recorded when there is no polarizer placed in the object arm. The vector properties are measured under different polarizations, with the polarizer placed after the q-plate (same as Fig. 4(e)). The results are given in Fig. 5(b)-5(d). The ICCD is set to fast external mode with an optical gate width of 5 ns. The triggered ghost images are obtained based on an accumulation of 500 exposures, with each exposure time being 1s. In the future, we also plan to investigate ghost imaging of vector Bessel beams and other vector beams.

Optics EXPRESS

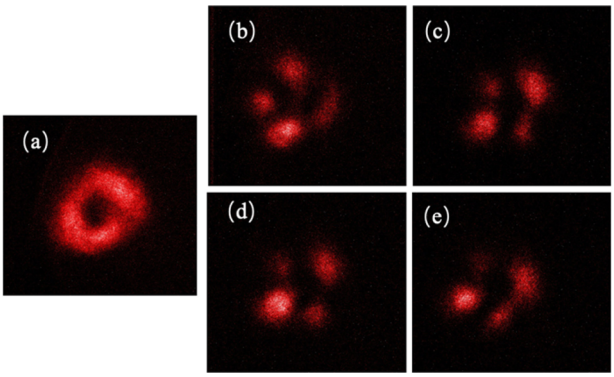

Fig. 5. Quantum ghost imaging of vector vortex beam with $m = 2$. (a) The observed ghost images with no polarizer placed before q-plate in the object arm. (b)–(e) The observed photon distributions of the ghost vector-vortex beam with P2 and as the polarization angle of P2 is 0°, 45°, 90° and 135°, separately.

3. Geometrical optics path explanation

In this section, we explain the experimental results of ghost vector imaging through Klyshko's advanced-wave picture. During the early work on ghost imaging, Klyshko proposed an intuitive model to predict the output of ghost imaging and it is widely used in the field [44,45]. Klyshko's advanced-wave representation considered the field detected in one arm as propagating in reverse back to the crystal plane, where it reflects off the crystal to propagate forward through the system to the image detector in the other arm. Aspden has experimentally demonstrated its validity [46]. Based on Klyshko's advanced-wave picture, the whole experimental configuration of ghost imaging can be tested by back-projection of a classical laser. Also, the ghost imaging results can be predicted.

Here, we illustrate the geometric path of our experimental setup with a simplified unwrapped schematic [22], as shown in Fig. 6(a). Then we present an equivalent model to predict the ghost vector vortex imaging configuration. As shown in Fig. 6(b), the single-pixel heralding detector is conceptually replaced with a light source, and the optical path is unwrapped.

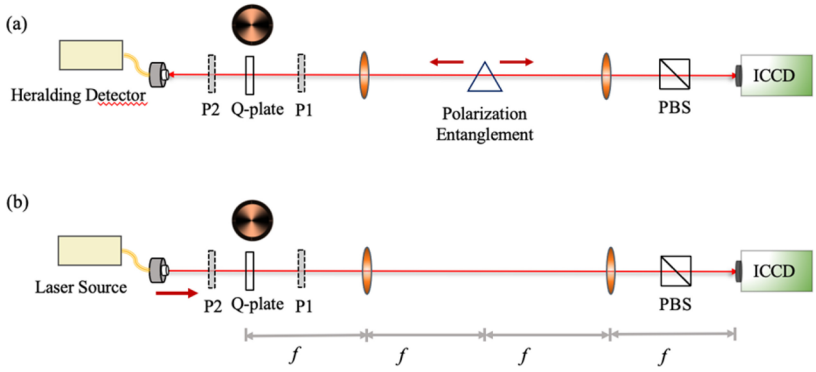

Fig. 6. (a) Simplified unwrapped schematic of ghost vector vortex imaging. (b) An equivalent model of our ghost imaging system.

From the geometrical optics path point of view, the laser illuminates onto the q-plate, and the imaging detector ICCD records the final distribution. The laser is arbitrarily polarized with both

Optics EXPRESS

H and *V* components. For the first case (Fig. 3), the polarizer P1 is placed after the *q*-plate. The photon state is a mixture of radically polarized and azimuthally polarized vector vortex states. The image reached at ICCD shows a donut distribution. For the second case, the polarizer P2 is placed before the *q*-plate, allowing only a linearly-polarized component to incident on the *q*-plate. This results in a vector beam distribution, with the PBS, a distribution of two petals is expected at ICCD plane. As discussed above, the results of vector ghost images can be well predicted through Klyshko's advanced-wave picture.

4. Conclusion

In this paper, we have successfully demonstrated the quantum ghost imaging of vector vortex images and provided a corresponding theoretical analysis. We also give the geometrical optics path explanation of ghost vector imaging. In principle, our proposed method can also be used to generate the ghost imaging of other kinds of vector beams. For example, vector Bessel beam can be generated with the help of novel planar Pancharatnam-Berry phase optical elements [47,48], With proper design of the parameters of the object, ghost imaging of vector Bessel beams can be achieved. In the future, we also plan to investigate ghost imaging of vector Bessel beams and other vector beams.

Quantum ghost imaging technology has a wide range of application prospects in materials science, biomedicine, and other fields. By expanding the principle of ghost imaging to spatially varying vector beams, we can expect interesting developments in this area. In contrast to traditional ghost imaging experiments which mainly focus on amplitude objects and simple phase objects, our method of generating vector ghost imaging enables the study of complex structured light. Ghost imaging of structured light may have applications in imaging universal motion vectors in the natural world and human industry. Furthermore, considering the exciting development in the field of quantum imaging [49], such as imaging with undetected photons, and interaction- free measurement [23,50,51], this work may find new applications.

Funding. National Key Research and Development Program of China (2022YFA1405000, 2019YFA0308700); Innovation Program for Quantum Science and Technology (2021ZD0301400, 2021ZD0301500); National Natural Science Foundation of China (61975077, 62222507, 92365107, 12305020); Natural Science Foundation of Jiangsu Province (BK20212004); Program for Innovative Talents and Entrepreneurs in Jiangsu (JSSCTD202138); China Postdoctoral Science Foundation (2023M731613); Jiangsu Funding Program for Excellent Postdoctoral Talent (2023ZB708).

Disclosures. The authors declare no conflicts of interest.

Data availability. Data underlying the results presented in this paper are not publicly available at this time but may be obtained from the authors upon reasonable request.

References

1. M. J. Padgett and R. W. Boyd, "An introduction to ghost imaging: quantum and classical," Philos. Trans. R. Soc., A **375**(2099), 20160233 (2017).
2. P.-A. Moreau, E. Toninelli, T. Gregory, *et al.*, "Ghost Imaging Using Optical Correlations," Laser Photonics Rev. **12**(1), 1700143 (2018).
3. W. Li, Z. Tong, K. Xiao, *et al.*, "Single-frame wide-field nanoscopy based on ghost imaging via sparsity constraints," Optica **6**(12), 1515 (2019).
4. B. Sun, M. P. Edgar, R. Bowman, *et al.*, "3D Computational Imaging with Single-Pixel Detectors," Science **340**(6134), 844–847 (2013).
5. C. Zhang, Y. Wang, Y. Yin, *et al.*, "High precision 3D imaging with timing corrected single photon LiDAR," Opt. Express **31**(15), 24481 (2023).
6. G. Wang, H. Zheng, Z. Tang, *et al.*, "All-Optical Naked-Eye Ghost Imaging," Sci. Rep. **10**(1), 2493 (2020).
7. S. Yuan, J. Yao, X. Liu, *et al.*, "Cryptanalysis and security enhancement of optical cryptography based on computational ghost imaging," Opt. Commun. **365**, 180–185 (2016).
8. D. Pelliccia, A. Rack, M. Scheel, *et al.*, "Experimental X-Ray Ghost Imaging," Phys. Rev. Lett. **117**(11), 113902 (2016).
9. A.-X. Zhang, Y.-H. He, L.-A. Wu, *et al.*, "Tabletop x-ray ghost imaging with ultra-low radiation," Optica **5**(4), 374 (2018).
10. R. I. Khakimov, B. M. Henson, D. K. Shin, *et al.*, "Ghost Imaging with Atoms," Nature **540**(7631), 100–103 (2016).

Optics EXPRESS

11. S. Li, F. Cropp, K. Kabra, *et al.*, "Electron Ghost Imaging," Phys. Rev. Lett. **121**(11), 114801 (2018).
12. T. B. Pittman, Y. H. Shih, D. V. Strekalov, *et al.*, "Optical imaging by means of two-photon quantum entanglement," Phys. Rev. A **52**(5), R3429–R3432 (1995).
13. D. V Strekalov, A. V. Sergienko, D. N. Klyshko, *et al.*, "Observation of Two-Photon "Ghost" Interference and Diffraction," Phys. Rev. Lett. **74**(18), 3600–3603 (1995).
14. D. N. Klyshko, "Two-photon light: Influence of filtration and a new possible EPR experiment," Phys. Lett. A **128**(3-4), 133–137 (1988).
15. J. C. Howell, R. S. Bennink, S. J. Bentley, *et al.*, "Realization of the Einstein-Podolsky-Rosen Paradox Using Momentum- and Position-Entangled Photons from Spontaneous Parametric Down Conversion," Phys. Rev. Lett. **92**(21), 210403 (2004).
16. R. S. Aspden, D. S. Tasca, R. W. Boyd, *et al.*, "EPR-based ghost imaging using a single-photon-sensitive camera," New J. Phys. **15**(7), 073032 (2013).
17. D. S. Tasca, R. S. Aspden, P. A. Morris, *et al.*, "The influence of non-imaging detector design on heralded ghost-imaging and ghost-diffraction examined using a triggered ICCD camera," Opt. Express **21**(25), 30460 (2013).
18. X. Qiu, D. Zhang, T. Ma, *et al.*, "Parallel Ghost Imaging," Adv. Quantum Technol. **3**(10), 2000073 (2020).
19. X. Qiu, D. Zhang, W. Zhang, *et al.*, "Structured-Pump-Enabled Quantum Pattern Recognition," Phys. Rev. Lett. **122**(12), 123901 (2019).
20. C. Moodley and A. Forbes, "Super-resolved quantum ghost imaging," Sci. Rep. **12**(1), 10346 (2022).
21. R. Borghi, F. Gori, and M. Santarsiero, "Phase and amplitude retrieval in ghost diffraction from field-correlation measurements," Phys. Rev. Lett. **96**(18), 183901 (2006).
22. R. S. Aspden, P. A. Morris, R. He, *et al.*, "Heralded phase-contrast imaging using an orbital angular momentum phase-filter," J. Opt. **18**(5), 055204 (2016).
23. Y. Zhang, A. Sit, F. Bouchard, *et al.*, "Interaction-free ghost-imaging of structured objects," Opt. Express **27**(3), 2212 (2019).
24. A. Saxena, M. Kaur, V. Devrari, *et al.*, "Quantum ghost imaging of a transparent polarisation sensitive phase pattern," Sci. Rep. **12**(1), 21105 (2022).
25. B. Sephton, I. Nape, C. Moodley, *et al.*, "Revealing the embedded phase in single-pixel quantum ghost imaging," Optica **10**(2), 286 (2023).
26. H. Kellock, T. Setälä, A. T. Friberg, *et al.*, "Polarimetry by classical ghost diffraction," J. Opt. **16**(5), 055702 (2014).
27. S. Dongfeng, Z. Jiamin, H. Jian, *et al.*, "Polarization-multiplexing ghost imaging," Opt. Lasers Eng. **102**, 100–105 (2018).
28. A. S. Chirkin, P. P. Gostev, D. P. Agapov, *et al.*, "Ghost polarimetry: ghost imaging of polarization-sensitive objects," Laser Phys. Lett. **15**(11), 115404 (2018).
29. D. Shi, S. Hu, and Y. Wang, "Polarimetric ghost imaging," Opt. Lett. **39**(5), 1231 (2014).
30. M. Rosskopf, T. Mohr, and W. Elsäßer, "Ghost Polarization Communication," Phys. Rev. Appl. **13**(3), 034062 (2020).
31. A. Vega, T. Pertsch, F. Setzpfandt, *et al.*, "Metasurface-Assisted Quantum Ghost Discrimination of Polarization Objects," Phys. Rev. Appl. **16**(6), 064032 (2021).
32. S. Magnitskiy, D. Agapov, and A. Chirkin, "Quantum ghost polarimetry with entangled photons," Opt. Lett. **47**(4), 754 (2022).
33. J. Chen, C. Wan, and Q. Zhan, "Vectorial optical fields: recent advances and future prospects," Sci. Bull. **63**(1), 54–74 (2018).
34. C. Maurer, A. Jesacher, S. Fürhapter, *et al.*, "Tailoring of arbitrary optical vector beams," New J. Phys. **9**(3), 78 (2007).
35. A. Forbes, "Structured Light from Lasers," Laser Photonics Rev. **13**(11), 1900140 (2019).
36. L. Marrucci, C. Manzo, and D. Paparo, "Optical Spin-to-Orbital Angular Momentum Conversion in Inhomogeneous Anisotropic Media," Phys. Rev. Lett. **96**(16), 163905 (2006).
37. E. Nagali, F. Sciarrino, F. De Martini, *et al.*, "Quantum Information Transfer from Spin to Orbital Angular Momentum of Photons," Phys. Rev. Lett. **103**(1), 013601 (2009).
38. T. Kim, M. Fiorentino, and F. N. C. Wong, "Phase-stable source of polarization-entangled photons using a polarization Sagnac interferometer," Phys. Rev. A **73**(1), 12316 (2006).
39. Z.-X. Li, D. Zhu, P.-C. Lin, *et al.*, "High-dimensional entanglement generation based on a Pancharatnam–Berry phase metasurface," Photonics Res. **10**(12), 2702 (2022).
40. Z.-X. Li, Y.-P. Ruan, J. Tang, *et al.*, "Self-healing of a heralded single-photon Airy beam," Opt. Express **29**(24), 40187 (2021).
41. A. Mair, A. Vaziri, G. Weihs, *et al.*, "Entanglement of the orbital angular momentum states of photons," Nature **412**(6844), 313–316 (2001).
42. G. Milione, S. Evans, D. A. Nolan, *et al.*, "Higher Order Pancharatnam-Berry Phase and the Angular Momentum of Light," Phys. Rev. Lett. **108**(19), 190401 (2012).
43. G. Milione, H. I. Sztul, D. A. Nolan, *et al.*, "Higher-Order Poincaré Sphere, Stokes Parameters, and the Angular Momentum of Light," Phys. Rev. Lett. **107**(5), 053601 (2011).
44. T. B. Pittman, D. V. Strekalov, D. N. Klyshko, *et al.*, "Two-photon geometric optics," Phys. Rev. A **53**(4), 2804–2815 (1996).

Optics EXPRESS

45. D.-Z. Cao, J. Xiong, and K. Wang, "Geometrical optics in correlated imaging systems," Phys. Rev. A **71**(1), 013801 (2005).
46. R. S. Aspden, D. S. Tasca, A. Forbes, *et al.*, "Experimental demonstration of Klyshko's advanced-wave picture using a coincidence-count based, camera-enabled imaging system," J. Mod. Opt. **61**(7), 547–551 (2014).
47. A. Niv, G. Biener, V. Kleiner, *et al.*, "Propagation-invariant vectorial Bessel beams obtained by use of quantized Pancharatnam–Berry phase optical elements," Opt. Lett. **29**(3), 238 (2004).
48. A. Dudley, Y. Li, T. Mhlanga, *et al.*, "Generating and measuring nondiffracting vector Bessel beams," Opt. Lett. **38**(17), 3429 (2013).
49. P.-A. Moreau, E. Toninelli, T. Gregory, *et al.*, "Imaging with quantum states of light," Nat. Rev. Phys. **1**(6), 367–380 (2019).
50. J. R. Hance and J. Rarity, "Counterfactual ghost imaging," npj Quantum Inf. **7**(1), 88 (2021).
51. Y. Yang, H. Liang, X. Xu, *et al.*, "Interaction-free, single-pixel quantum imaging with undetected photons," npj Quantum Inf. **9**(1), 2 (2023).